This is a repository copy of *Phase transformation of Sn-based nanowires under electron beam irradiation*.

White Rose Research Online URL for this paper:
http://eprints.whiterose.ac.uk/93842/

Version: Accepted Version

Journal of
Materials Chemistry C

Materials for optical and electronic devices
www.rsc.org/materialsC

Volume 1 | Number 1 | Jan 2013 | Pages 1–100

ROYAL SOCIETY
OF CHEMISTRY

ROYAL SOCIETY
OF CHEMISTRY

www.rsc.org/materialsC

Journal Name

Dynamic Article Links ▶

ARTICLE TYPE

Phase Transformation of Sn-based Nanowires under Electron Beam Irradiation

Hong Zhang, ‡[a] Xia Deng, ‡[a] Junwei Zhang,[a] Desheng Xue,[a] Yuanqing Huang,[a] Feiming Bai,[b] Beverly. J. Inkson[c] and Yong Peng*[a]

One dimensional metal phase-change nanomaterials provide a valuable research platform for understanding nanoscale phase transformation behavior and thermal properties, which have potential applications into identification system such as information storage, barcoding, and detection. Sn-based 10 nanowires fabricated by a DC electrodeposition technique into nanoporous templates are irradiated by an electron beam in situ a transmission electron microscopy. With the assitance of oxide shell covered on the Sn-based nanowires, periodic and non-periodic multilayered nanostructures are precisely sculpted and the reversibility between original homogeneous alloy phase and precipitated phases is controllable. The formation mechanism of the phase reversibility and sculpting process also work on other phase-change 15 materials, proved by using individual SnPb alloy nanowires as test. A single Sn-Ag alloy nanowire with several micron in length is proved to be easily coded into dozens of morphology/phase status, which can produce more than 1000 barcodes. This controllable phase tunable strategy via selective e-beam irradiation enignering technique is blieve to open up a way of sculpting an individual nanowire with various phase status and periodicities, which may encode into a promising micro-nano identification 20 system with the advantages of ultrahigh capacity, sustainable utilization and well stability.

Introduction

Phase-change materials (PCMs) which have the properites of large latent heats of fusion and sharp melting point[1] have been used in heat mamagement purposes including direct thermal 25 energy storage such as sports wear, bedding accessories and home textiles,[2, 3] solar energy applications especially in space,[4] conditioning of buildings[5] and medical applications [6]. In the recent developments, they have been re-discovered and successfuly expanded into the various fields of high-technologies, 30 such as information storage,[7-9] smart drug delivery,[10-12] detection[13-15] and covert identification system[16, 17].

An unmet need is to develop micro-nanoscale covert identification system that can be used to tag trading objects and forensic investigation by tracing a specific object to its 35 manufacturer, vendor or purchaser[18]. This is because macroscopic barcodes are dimensionally mismatched with product and always visible, which can be altered or duplicated for counterfeiting and unlawful use[19]. Advances in nanotechnologies have opened the possibility of creating ultrahigh capacity covert or invisible 40 taggants identification system by taking the dimension advantage of nanostructured materials, where they can be encode and decode through their unique physical signatures such as electric[20], heat[17], magnetic[21], optical[22-24], or electrochemical properties[25]. However, the lack of unique physical property of an individual

nano-block restricts their ability to label each object in a series[15], 45 which means that one type of nano-unit cannot be distinguished from each other based on above physical signatures.

In the view of tradtional knowledge, metals are not considered to be good PCMs because of their high densities and relatively 50 high melting points. However, the development of technology for the fabrication of nanomaterials has made metal PCMs substantially more viable because their melting points are proved to obviously reduce at the nanoscale.[26] Moreover, metals also have the advantages of high thermal conductivity, high density 55 latent heat storage capability, good thermal cycling stability, slight super-cooling and sharp, well-defined melting behaviors,[27] all of which are attractive for a number of applications, especially as absorptive heat sinks in electronic devices.[28] In addition, the rich metallurgic knowledge that has been accumulated over the 60 past hundred years enables easy design of metal PCM alloys with controlled melting points and latent heats. Among them, metals with low melting points (Sn,[29] Bi,[30] Pb,[31] In,[32] Cd,[33] Ge[34] and their alloys) are of particular interest.[1]

Sn-based alloys as one group of low-melting point PCMs are 65 commonly used as solders in welding due to their outstanding flowing property, low melting point, good corrosion resistance, and a certain extent of strength and relatively high conductivity.[35, 36] Our previous works have demonstrated that 1D Sn99Au1[37] and Sn-3.5Ag[38] nanosolders functions well in nanoscale electrical 70 nanowelding. Considering the extensive applications of metal PCMs, we have investigated the phase transformation of Sn-

based alloy nanowires under transmission electron microscopy (TEM) electron beam irradiation (EBI) in this work.

Transmission electron microscopy (TEM) is an essential and powerful tool commonly used to analyze nanomaterials. It can not only provide a deep insight into atomic-level observation, but also dynamical physical- or chemical- mechanism including in situ phase/shape transformation, molten nanofluid migration and electromigration. Further investigations demonstrate that this tool can be used into nanoengineering. In general, the irradiation of solids with energetic particles is thought to introduce defects and thus deteriorates the materials, which is normally an undesirable phenomenon.[39-41] But recent experiments on electron or ion irradiation of various nanostructures demonstrate that the irradiation can induce several unexpected beneficial effects, which allows tailoring the morphology, structure and properties of the material at the nanoscale.[42-46] Nevertheles, the engineering of nanostructures by EBI is usually inhomogeneous or with poor spatial periodicity due to the development limitation of electron beam sources and poor maneuverability.

In this work, we demonstrate a novel promising application of Sn-based alloy nanowires based on the properties of their phase transformation under EBI inside an ultra-high-vacuum TEM. In order to avoid a complete reflow under EBI and realize the engineering of the Sn-based nanowires at the nanoscale, a thin oxide layer was intended to grow on the surface of these nanowires by thermal oxidation treatment for providing a pipe-like spatial confinement. The irradiation experiments show that SnAg and SnPb alloy nanowires can be engineered into concentrational stratification structure, where size and position of the precipitated phases also could be tunable via selective EBI. By means of this phase-change behavior, a controllable reversibility between homogeneous alloy and precipitated phases and a sculpting of ordered nano-patterns at the nanoscale are realizable. It is proved that an individual Sn-based alloy nanowire with several micron in length can be encoded into more than 1000 barcodes, which is a very promising ultrahigh capacity micro/nano identification system.

Experimental details

Preparation of 1D Sn-Ag and Sn-Pb alloy nanowires

Sn-Ag alloy nanowires and Sn-Pb alloy nanowires were fabricated by a DC electrodeposition technique using anodic aluminum oxide (AAO) and polycarbonate (PC) templates with about 80 nm diameter pores. The electrodeposition was achieved in a three-electrodes glass cell on a electrochemical workstation (CHI 660E, CHI Instruments Co., China) at room temperature, in which the packaged template was used as working electrode, the reference electrode was a saturated calomel electrode (SCE) and the counter electrode was a platinum plate. The detailed preparation process of AAO templates and Sn-Ag alloy nanowires are introduced in our previous work.[38] Sn-Ag electrodeposition electrolyte composed of 0.30 M $Sn(CH_3SO_3)_2$, 4.5 mM AgI, 0.60 M $K_4P_2O_7$, 1.0 M KI, 0.4 M TEA, 6.4 mM heliotropin (HT) and 2 g/L hydroquinone. A -0.8 V potential was applied to obtain 1D Sn-Ag alloy nanowires. Sn-Pb electrodeposition electrolyte composed of 0.30 M $Sn(CH_3SO_3)_2$, 0.30 M $Pb(CH_3SO_3)_2$, 2 g/L ascorbic acid, 10 g/L sodium
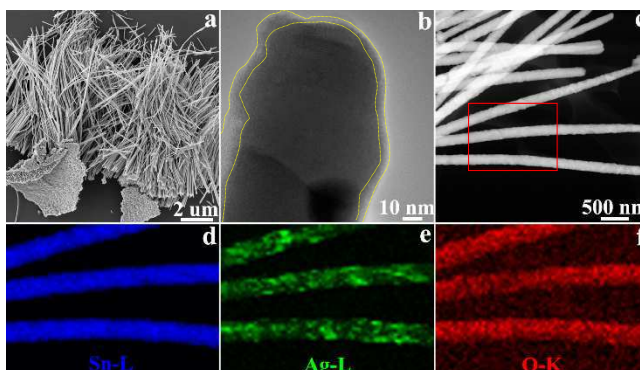

Figure 1. Morphologies of Sn-Ag nanowirs before and after thermal oxidation treatment. (**a**) SEM image of bundles of fresh prepared Sn-Ag nanowirs, of which AAO templates have been fully dissolved. (**b**) TEM image of a representative Sn-Ag nanowire after thermal oxidation treatment, with an approximate 4~10 nm oxide layer on the surface. (**c**) HAADF-STEM image of oxidized Sn-Ag nanowires with the existence of large size precipitation. (**d-f**) The corresponding EDX elemental mappings of O-K, Ag-L and Sn-L from nanowires marked by red rectangle.

hypophosphite and 2 g/L hydroquinone. A -0.5 V potential was applied to obtain 1D Sn-Pb alloy nanowires. The pH value of the electrodeposition electrolyte was adjusted to 5.5-6.0 by adding methanesulfonic acid. After elctrodeposition, the AAO templates or PC templates were completely dissolved in 0.1 M sodium hydroxide solution or dichloromethane for releasing nanowires, which are then rinsed with distilled water and dispersed on holey carbon coated copper grids for TEM analysis. The as-prepared Sn-based nanowires were then put in a tube funace (OTF-1200X, HEFEI KE JING Materials Technology Co., China) and heated to 150 ºC for 2h in air to thermal oxidize the surface layers of nanoiwres.

Characterization and EBI

The morphology, structure, chemistry and in-situ irradiation experiments of Sn-Ag and Sn-Pb nanowires were performed on high-resolution field emission transmission electron microscopy (HRTEM, TecnaiTM G2 F30, FEI) operating at 300 keV with an emission current of 82 uA, equipped with energy dispersive x-ray spectroscopy (EDX, AMETEK Co., USA), selected area electron diffraction (SAED) and high angle annular dark field and scanning transmission electron microscopy (HAADF-STEM). X-ray diffraction (XRD, Philips X'pert Pro MPD (Cu Kα radiation), the Netherlands) instrument was employed to study the crystallographic properties. Since it is hard to record real-time images during the EBI processes because of the extremely high beam intensity, we took bright field TEM (BFTEM) images under normal conditions before and after every EBI.

Results and discussions

Morphologies of Sn-Ag nanowires before and after thermal oxidation

The morphologies of Sn-Ag nanowirs before and after thermal oxidation were observed by SEM and HAADF-STEM. Figure 1(a) shows a representative SEM image of a bundle of fresh

prepared SnAg nanowires, from which the AAO template has been completely dissolved. The size statistics reveals that the average diameter of the prepared SnAg nanowires is approximately 80 nm, the average length is around 10 μm. Further HAADF-STEM image (Figure S1a) shows that their surfaces are smooth and do not show obvious defects, revealing a good qualify. Quantitative analysis of EDX spectrum (Figure S1b) reveals that the chemical composition of the SnAg nanowires is a 78:22 weight ratio of Sn:Ag, referring a $Sn_{78}Ag_{22}$ chemical composition. EDX elemental mappings in Figure S1c-e show that the elements of Sn and Ag are nearly evenly distributed throughout the whole nanowires, indicating a uniform $Sn_{78}Ag_{22}$ chemical phase. XRD patterns of the fresh prepared Sn-Ag nanowires embedded in template (Figure S1b) indicates the successful alloying of Sn and Ag during the synthesis process, which can be matched to tetragonal β-Sn and orthorhombic Ag_3Sn. This was further confirmed through their crystal structures by HRTEM and CBED.

Figure 1(b) shows a TEM image of a Sn-Ag nanowire after thermal treatment, of which contrast clearly reveals a stratified structure. The grey layer coved on the nanowire surface and marked by false yellow curve is oxide with 4~10 nm thickness, which was measured to be SnO_2 (see supplementary Figure S2 for details). Figure 1(c) shows the HAADF-STEM image of the oxidized Sn-Ag nanowires. The contrast of HAADF-STEM images directly depends on the atomic number and thickness of the materials. It is seen that the brightness of nanowires has an obvious uneven distribution, indicating a non-uniform chemical phase of nanowires after thermal treatment. EDX elemental mapping technique was further adapted to quantitatively analyse the chemical element distribution. It is seen that the element Sn is
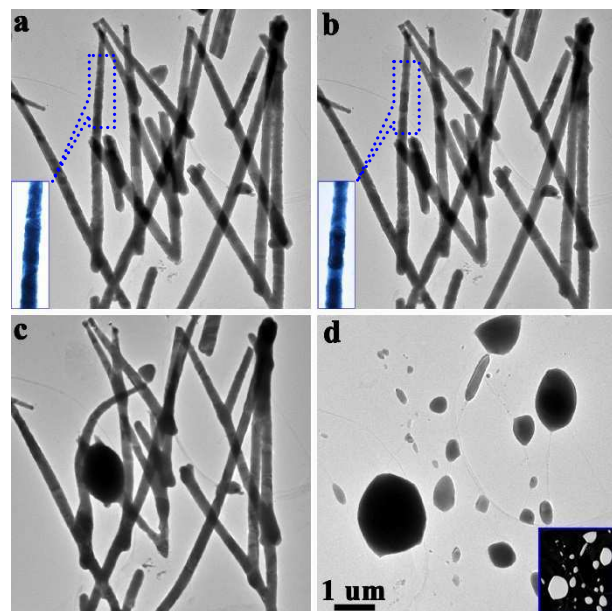
nearly evenly distributed throughout the whole nanowires, and the Ag has obvious aggregation. The intrinsic reason is deduced to originate from the abnormal growth of Ag_3Sn grains during the thermal oxidation process. The even distribution of oxygen element demonstrates the existence of oxide on the surface of nanowires after oxidation, and reveals that the surfaces of the individual 1D Sn-Ag nanowires have been successfully oxidized.

Reflowing properties of fresh prepared nanowires under EBI

Figure 2a shows a representative in situ irradiation experiment of a bundle of fresh prepared Sn-Ag nanowires. The diameter of the electron beam spot was about 5.8 μm with a $\sim 2.62 \times 10^{-2}$ A/cm^2 current density. The electron irradiation on nanowires is expected to give rise to energy transfer and induce a local increase in the temperature of the material. The induced temperature relies on several parameters, including e-beam spot size, electron acceleration voltage, exposure time and thermal conductivity of irradiated materials.[46, 47] When the nanowire region was exposed for the first 30 s as showed in Figure 2b, the $Sn_{78}Ag_{22}$ nanowires nearly remained their initial contour features under low-magnification observation. However, if we observed these features at high magnification, changes of phase/shape as marked by blue circles (the inset of Figure 2b) can be seen, revealing that the temperature of the nanowires induced by the electron beam irradiation has approached their melting point at this stage. After 32 s irradiation, the nanowires appeared bending deformation, and the morphology of some region had dramatically changed from the wire shape into spheroid shape as shown in Figure 3c. When the irradiation lasted 1 s more (Figure 3d), a complete reflow was led to. During this process, it was dynamically observed that the nanowires around the initial sphere and deformation parts as shown in Figure 3c started reflowing, and then taking part in binary collisions accompanied by liquid-like coalescence of the initial spheroid. The initial molten crystals grow at the expense of surrounding little crystals due to the minimized surface energy at liquid phase. It is also found that coalescence only occurs among particles, of which spaces are typically less than 1-2 nm.[48] If the gaps between the formed crystals are large enough like the situation of Figure 3d, the eventual morphology of the reflow remains unchanged even irradiated more time or stronger e-beam intensity. This irradiation reflow experiment in situ HRTEM demonstrates that our fresh prepared Sn-Ag alloy nanowires before thermal oxidation can accomplish a complete phase transformation from wires to particles under e-beam irradiation.

Forming concentrational stratification structure under EBL engineering

Although Sn-based nanowires are typical phase-change materials, the fresh prepared $Sn_{78}Ag_{22}$ nanowires completely reflows from the wire shape to spheroid shape within tens of seconds under EBI as observed in above section. It means that the fresh Sn-Ag nanowires cannot be tailored their morphologies, structures and physical properties at the nanoscale because of a lack of spatial confinement. In order to realize the engineering of the Sn-Ag nanowires at the nanoscale, the fresh $Sn_{78}Ag_{22}$ nanowires was intended to oxidize a thin layer oxide outside by annealed at 150 ºC for 2h in air. The oxide layer can withstand the heating, alike a heat barrier, and provide a pipe-like confinement due to its high

Figure 2. Morphological and structural evolution of a bundle of fresh prepared Sn-Ag nanowires under EBI revealing a good reflowing performance. **(a)** Initial TEM micrograph before irradiation. Inset, magnified view of blue region. **(b)** After 30 s of exposure. Inset, magnified view of blue region. **(c)** After 32 s of exposure. **(d)** After ~ 33 s of exposure. Inset, corresponding HAADF-STEM micrograph.
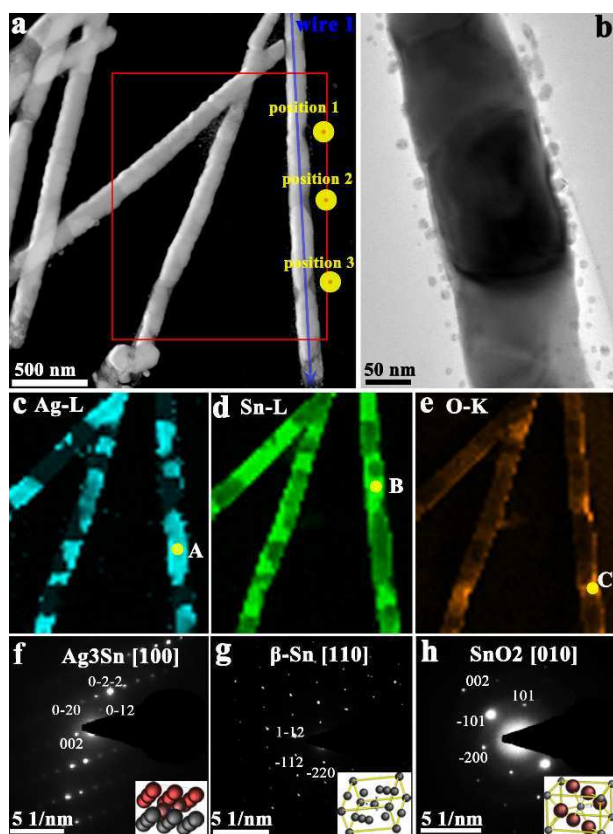
Figure 3. Mophological and structural evolution of a bundle of Sn$_{78}$Ag$_{22}$ alloy nanowires after thermal oxidation treatment under EBI. **(a)** HAADF-STEM image after EBI, showing that nanowire 1 has been sculpted into a phase-separation nanostructure. The yellow circles indicate the position of the e-beam spot. **(b)** The correspongding magnified BF-TEM image of naniwire 1 near position 2. **(c-e)** EDX elemental mappings of Sn-L, Ag-L and O-K from nanowires marked by red square. **(f-h)** CBED patterns coming from the A, B, and C three points marked by yellow in Figure 3c-e, respectively. Insets, the relevant crystal models.

melting temperature in comparison with its alloy, which creates a nanoscale condition to satisfy the phase separation of individual Sn$_{78}$Ag$_{22}$ nanowires. Figure 3a shows a HAADF-STEM image of the oxidized Sn$_{78}$Ag$_{22}$ nanowires after irradiated by a spread e-beam (beam spot was about 3 μm, current density is ~ 9.79×10^{-2} A/cm^2) at least 100 s until the inner alloy Sn$_{78}$Ag$_{22}$ became fluid, which flowed in the nano-pipe of SnO$_2$ oxide. Then a convergent e-beam (beam spot was about 60 nm, current density is ~ 1.93×10^2 A/cm^2) was sequentially placed at the position 1-3 marked by yellow circles to partly irradiate the nanowire. Figure 3b shows the corresponding magnified BF-TEM image of nanowire 1 near Position 2. It is can be seen that there is an obvious phase contrast along nanowire, reavling that the layered structures of concentrational stratifications have been formed at the edges of irradiation positions. The surfaces of individual nanowires clearly get a little bit rough. Especially, many nanoparticles with 2-8 nm diameter homogeneously distribute onto the carbon supporting film around the nanowire, which is result from loss of atoms by sputtering and redistribution of atoms by flow.

The chemical element distributions of Sn$_{78}$Ag$_{22}$ nanowires after EBI were further studied by HAADF-STEM, EDX linescan and EDX elemental mapping analysis techniques. Quantitative analysis of EDX spectrum (see supplementary Fig. S3a for details) reveals that the chemical composition of individual Sn$_{78}$Ag$_{22}$ nanowires has changed into Sn$_{80}$Ag$_{20}$. Figure S3b shows EDX line-scan spectra of Ag-Lα, Sn-Lα and O-Kα collected along blue line in Figure 3a, of which electron beam spot size was 1.5 nm. It is seen that the intensities of Sn, Ag and O are dramatically fluctuant, which indicate the changes of nanowire chemical compositions after EBI. Figure 3c-e further shows the EDX elemental mappings of Sn-Lα, Ag-Lα and O-Kα, respectively. The elements of Sn and Ag clearly appear aggregation, respectively. In addition, the oxygen mapping (Figure 3e) reveals that the electron beam irradiation also induced a further oxidization if a detailed comparison can be done before and after irradiation at position 1-3. The intrinsic reason originates from the existence of oxygen gas in the HRTEM chamber although it is a high vacuum. These results reveal that a phase change has occurred in individual Sn$_{78}$Ag$_{22}$ nanowires after EBI.

In order to accurately determine the chemical and structural states, the irradiated Sn-Ag nanowire was further examined by convergent beam electron diffraction (CBED) along the nanowire part by part. Figure 3f-3h show CBED patterns coming from the A, B, and C three points marked by yellow in Figure 3c-e, respectively, which can be well indexed into [100] crystallographic orientation of orthorhombic Ag$_3$Sn, [110] orientation of tetragonal SnO$_2$, and [010] orientation of body centered tetragonal (BCT) β-Sn, respectively. This result proves that the highlighted agglomerate phase is Ag$_3$Sn, the void is Sn phase, confirming that the phase separation has happened in the Sn$_{78}$Ag$_{22}$ nanowire under electron beam engineering.

According to the above observation and analysis of STEM morphology, EDX analysis and CBED detections, the intrinsic mechanism of the concentrational stratification of individual Sn$_{78}$Ag$_{22}$ nanowires under EBL engineering could be deduced. As it is known that the general solidification behavior of alloys in a simple binary eutectic system consists of two stages and involves a liquid (L) and two solid phases,[49] in our case, the primary stage would be L→Ag$_3$Sn in the range of temperatures from 480 ℃ (melting point of Ag$_3$Sn) to the binary eutectic of 221 ℃. Because the temperature of the irradiated nanowire near the irradiated positions 1-3 is higher than other part of this nanowire, the nucleation of Ag$_3$Sn was tended to avoid this irradiated region and began to solidify at the position away from the irradiated position. It is known that imperfections such as grain and interphase boundaries generally provide nucleation sites for phase changes,[49] thus the intermetallic phase Ag$_3$Sn was first formed along the pipe wall，and then individual particles diffuse across the surface and collide with other particles, leading to coalescence until the temperature cooling to the eutectic point. The secondary stage would be L→Ag$_3$Sn +β-Sn. Since solid Sn is difficult to nucleate with a supercooling of ~20 °C,[49, 50] the liquid then becomes Sn-rich by the continued formation of the intermetallic until a certain temperature, of which all Sn-rich liquid will quickly solidify to solid β-Sn when the heat is further dissipated.
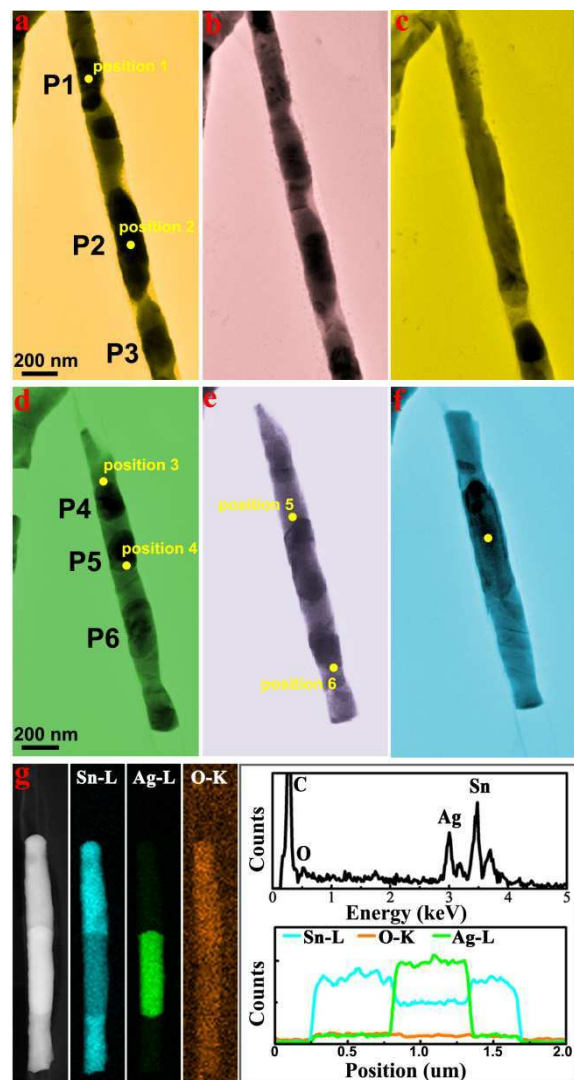
Figure 4. A reversibility steering strategy between homogeneous alloy phase and precipitated phases of SnAg piping system via site-selective EBI engineering. **(a-c)** Restoration of the precipitated phases into the original homogeneous alloy phase. The solid yellow dot indicates the position of the e-beam spot. **(d)** Re-formation of layered structure with three Ag3Sn precipitations marked as P4, P5 and P6, and **(e-f)** tunability of their size and position. **(g)** Chemical analysis of the representative phase status of Fig. 4e by EDX elemental mapping and line-scan analysis technique respectively.

Steering the phase transformation of Sn-based nanowires

After phase agglomeration, the separation phase of Ag_3Sn located in the middle of two Sn phases was extremely sensitive to the e-beam (beam spot was about 5 nm, current density is ~ 2.27×10^4 A/cm^2). Even a very short irradiation time (~1 s) could drive it to quickly flow in channel, just the same as the Sn phases. By means of this phase-change behavior, reversibility between homogeneous alloy and precipitated phases is controllable via the selective e-beam irradiation. Furthermore, a sculpting of ordered nano-patterns is realizable.

Figure 4a-4c demonstrates how the EBI technique is used to precisely control the phase reversibility of the $Sn_{78}Ag_{22}$ nanowire between precipitated phases and homogeneous alloy at the nanoscale. Figure 4a is the corresponding bright-field TEM image of the nanowire 1 shown in Figure 3a, which has completed the first stage of section cuttings. It is seen that the body of this Sn-Ag nanowire has a vivid contrast, which has appeared concentrational stratification structure as discussed above. The dark contrasts show three Ag_3Sn precipitated phases as marked P1, P2, and P3. After electron beam was irradiated on position 1 and 2 for 10 s back and forth several times, it was observed that the Ag_3Sn precipitated phases of P1 and P2 (Figure 4b) diffused with β-Sn precipitated phase in the oxide pipe and left the irradiated region. The contrast of the single $Sn_{78}Ag_{22}$ nanowire eventually became even again as shown in Fig. 4c, which reveals a disappearance of the concentrational stratification and a reappearance of homogeneous alloy phase. Combined with the first stage in Figure 3, this result proves that the homogeneous alloy phase and precipitated phases of the PCM $Sn_{78}Ag_{22}$ nanowire are reversible under EBI.

The EBI technique also realizes a fusion of the Ag_3Sn precipitated phases, and their size- and position- changes at the nanoscale. Figure 4d-4f shows a reformed layered structure with three Ag3Sn precipitations marked as P4, P5 and P6 in the same nanowire by means of the EBI method. When the electron beam was successively placed on position 3, 4 (Fig. 4e), 5 and 6 (Fig. 4f), the three Ag_3Sn precipitations can be easily driven and fused together as shown in Fig. 4f. Quantitative analysis of EDX

Figure 5. Sculpting of ordered nano-patterns via the EBI technique. **(a)** Layered structure with one integral Ag_3Sn precipitations, **(b)** two periodic Ag_3Sn precipitations, **(c)** three periodic Ag_3Sn precipitations and **(d)** three non-periodic Ag_3Sn precipitations. **(e)** The elemental distributions and quantitative analysis of EDX show that the black layers in Fig. 5d are Ag_3Sn and the grey layers are β-Sn.
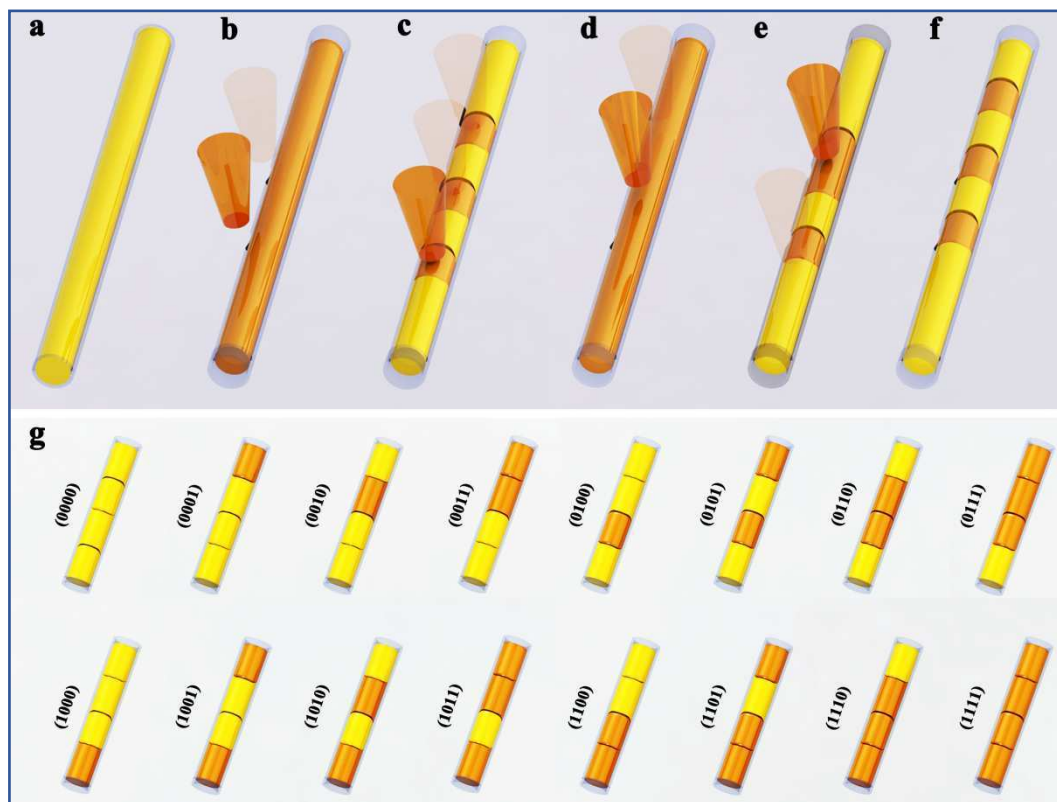
Figure 6. **(a-f)** Schematic diagram of the formation mechanism of the phase reversibility and sculpting process of the phase-change SnAg nanowires. **(g)** Schematic diagram of the encoding process of an individual SnAg nanowire, where Ag$_3$Sn precipitated layers can be encoded into '1' and rich β-Sn layers is encoded into '0'.

spectrum and investigation of chemical elemental distributions prove that the fused integral precipitation (bright section in HAADF-STEM image of Fig. 4g) remains the Ag$_3$Sn phase and the grey sections in HAADF-STEM image of Fig. 4g remains β-Sn phase.

Both the precise control of phase reversibility and adjustment of precipitated phases are achievable. Figure 5a-5c demonstrates how the EBI technique is intended to precisely tailor nano-patterns by utilizing the phase-change property of the single Sn$_{58}$Ag$_{42}$ nanowire. Fig. 5b shows that the structure in Fig. 5a (or Fig. 4f) has been further sculpted into a periodic layered structure with two Ag$_3$Sn layers and three β-Sn layers by irradiating the middle of the integral Ag$_3$Sn precipitation for about 1 s. Fig. 5c shows another periodic layered structure with three Ag$_3$Sn layers and four β-Sn layers, which was further engineered on the basis of Fig. 5b. Besides, non-periodic structure can be engineered. As an example, Fig. 5d shows a non-periodic structure by irradiating the periodic structure of Fig. 5c. The elemental distributions and quantitative analysis of EDX (Fig. 5e) also show that the black layers in Fig. 5d are Ag$_3$Sn and the grey layers are β-Sn.

On the basis of above experiments and observations, a formation mechanism of the phase reversibility and sculpting process of the phase-change Sn$_{78}$Ag$_{22}$ nanowires in this work is proposed, outlined in the schematic diagrams illustrated in Figure 6. It started from a single Sn$_{78}$Ag$_{22}$ alloy nanowire prepared by a DC electrodeposition technique. In order to avoid a complete reflow under EBI and realize the engineering of the Sn-Ag nanowires at the nanoscale, a thin oxide layer is intended to grow on the surface of the nanowire for providing a pipe-like spatial confinement (Figure 6a). The specimen is firstly irradiated by a spread e-beam until the inner alloy become fluid, which flows in the nano-pipe of SnO$_2$ oxide (Figure 6b). A convergent e-beam is then sequentially placed near the edge of the phase-change nanowires to determine the size of phase-separation layers. Concentrational stratification structure with alternating Ag$_3$Sn and rich-Sn phase will form when e-beam is moved away and temperature cools down enough (Figure 6c). After the cuttings of these sections, the layered nanostructures become sensitive to e-beam. By precisely controlling the irradiation position of e-beam or scanning the e-beam back and forth, the precipitated phases can be restored into the original homogeneous alloy phase, which realize a controllable reversibility between homogeneous alloy and precipitated phases (Figure 6d). If the e-beam is selectively placed onto the body of Ag$_3$Sn precipitations, the shapes and positions of the precipitated phases can be precisely steered (Fig. 6e). Ordered nano-patterns also therefore can be tailored as shown in Fig. 6f.

This mechanism describes a universal phase-change behavior of phase-change materials under electron beam irradiation, which is believed to also work on other phase-change materials similar with SnAg alloy. Sn-Pb alloy nanowires were therefore prepared and used to test the mechanism's universality, of which was also oxidized a thin layer oxide outside. As shown in Figure. S4, the homogeneous SnPb alloy can be quickly engineered into a multilayered nanostructure by EBI. Similar with the above Sn$_{78}$Ag$_{22}$ nanowire, the homogeneous SnPb alloy is also

restorable by scanning the e-beam among the precipitated phases back and forth several times. The elemental distributions and quantitative analysis of EDX prove the reversibility and controllability between the homogeneous phase and precipitated phases. The tailoring details can be seen in the supplementary Figure S4.

The Sn-Ag and Sn-Pb nanowire with several micrometers in length in Figure 4, Figure 5 and Figure S4 can be easily coded into dozens of morphology/phase status under the nano-engineerings of EBI, which could be used as an ultrahigh capacity identification system. In our case, the encoding capacity is dependent on the number of precipitated phases. Taking an individual Sn-based nanowire which can generate four Ag_3Sn precipitated phases as an example, the schematic illustration depicting the encoding process is presented in Figure 6g. The nanowire was engineered into four sections. Each section can be denoted as one or zero depending on whether the Ag_3Sn precipitated phase is generated or not. According to the combination rule, 15 combinations of four parts are 0000, 0001, 0010, 0011, 0100, 0101, 0110, 0111, 1000, 1001, 1010, 1011, 1100, 1101 and 1110 (Note that the combination 1111 corresponding to 0000 should be removed). Thus, the number of different barcodes can be derived graphically from Pascal's triangle using:

$$\sum_{k=1}^{n} C_n^k - 1 \approx \sum_{k=1}^{n} \frac{n!}{k!(n-k)!} = 2^n - 1 \qquad (1)$$

Where n is the total number of precipitated phases, and k is the number of precipitated phases in one permutation. From the equation, an individual nanowire with ten different phase statuses can produce 1023 barcodes; 40 different precipitated phases are able to generate more than 10^{12} different barcodes, which is sufficiently large for the most of the identification requirements. The phase transformation behaviors of one nanowire structure can be repeatable for many times, the long term stability of phase status at room temperature has been confirmed due to the existence of oxide layer outside. In comparison with the reported encoding strategies based on segmented nanowires[22-24], the encoding process and barcode numbers in our case are more flexible. In addition, the decoding process of our case is based on the phase contrast of TEM images, which is easier than those of the reported work by using optical reflection or light-emitting differences in specific instruments. All these advantages, including ultrahigh capacity, sustainable utilization and stability, demonstrate that Sn-Ag alloy core-shell nanowire structure is a very promising micro/nano identification system. Moreover, Sn-based alloy is commonly used in the connection of materials or devices as commercial solder. Combined with this unique identification feature, it enables us to identify of arms, ammunitions, vehicles and so on, which will play an important role on reconnoitering firearm related crime and managing military supplies.

Conclusions

In summary, a controllable phase manipulation strategy of Sn-based alloy nanowires with an oxide layer outside under EBI has been demonstrated. This strategy is based on the control of precipitated phases using an e-beam extracted from an ultra-high-vacuum TEM. By means of this phase-change behavior, sculpting ordered nano-patterns via this selective e-beam irradiation is realizable.

Individual Sn-Ag nanowires fabricated by a DC electrodeposition technique were selected as molel systems. The proposed method can also be applied to any Sn-based PCMs systems, which was proved by Sn-Pb nanowires. Our results demonstate that the enigneering technique via selective e-beam irradiation can tailor the PCMs in the nanoscale space. It is proved that an individual Sn-Ag alloy nanowire with 100 nm in diameter and several micron in length can be coded into dozens of morphology/phase status, which can produce more than 1000 barcodes. This micro-nano identification system, with ultrahigh capacity, sustainable utilization and well stability, may have important applications for metal PCMs in the nanoscale space, especially in reconnoitering firearm related crime and managing military supplies.
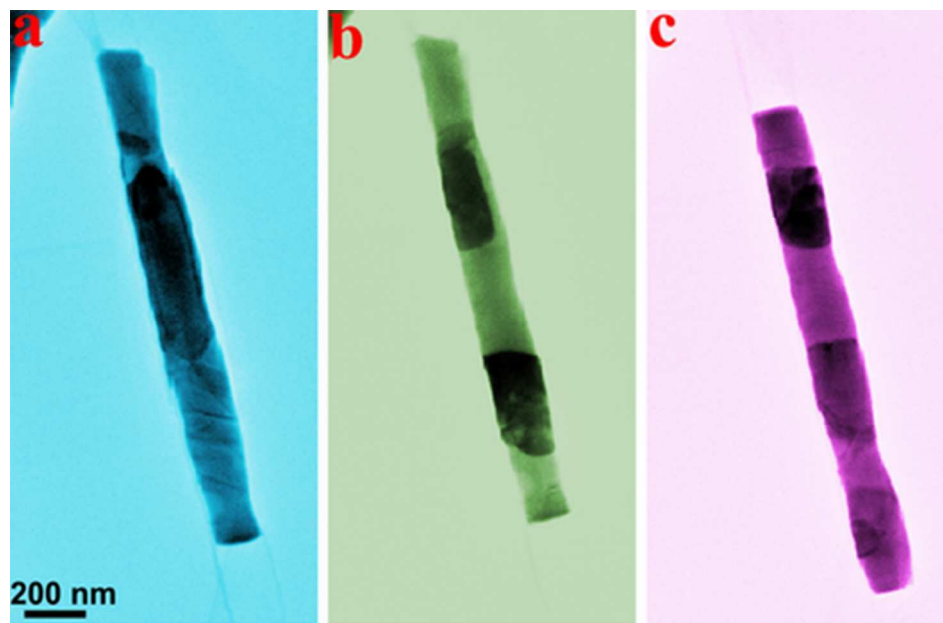
Acknowledgements

Notes and references

‡These authors contributed equally to this work.
a Key Laboratory of Magnetism and Magnetic Materials of Ministry of Education, Lanzhou University, Lanzhou 730000, P. R. China. E-mail: pengy@lzu.edu.cn; Fax: +86 9318912616; Tel: +86 13609310425
b State Key Laboratory of Electronic Thin Films and Integrated Devices, University of Electronic Science and Technology, Chengdu 610054, Sichuan, P. R. China. E-mail: fmbai@uestc.edu.cn
c Department of Materials Science and Engineering, University of Sheffield, Sheffield S1 3JD, UK. E-mail: beverley.inkson@sheffield.ac.uk

† Electronic Supplementary Information (ESI) available: [Chemical analysis of the $Sn_{78}Ag_{22}$ nanowires before thermal oxidation. Structural analysis of the outside oxide layer of the $Sn_{78}Ag_{22}$ nanowires. EDX spectrum and EDX linescan spectra of $Sn_{78}Ag_{22}$ nanowires in Figure 3. Steering the phase transformation behavior of Sn-Pb alloy nanowires]. See DOI: 10.1039/b000000x/

1. D. C. Hyun, N. S. Levinson, U. Jeong and Y. Xia, *Angew. Chem. Int. Edit.*, 2014, **53**, 3780-3795.
2. F. Agyenim, N. Hewitt, P. Eames and M. Smyth, *Sust. Energ. Rev.*, 2010, **14**, 615-628.
3. S. Mondal, *Applied Thermal Engineering*, 2008, **28**, 1536-1550.
4. M. Kenisarin and K. Mahkamov, *Renew. Sust. Energ. Rev.*, 2007, **11**, 1913-1965.
5. F. Kuznik, D. David, K. Johannes and J.-J. Roux, *Renew. Sust. Energ. Rev.*, 2011, **15**, 379-391.
6. A. Sari, A. Karaipekli, R. Eroğlu and A. Biçer, *Energy Sources, Part A: Recovery, Utilization, and Environmental Effects*, 2013, **35**, 1285-1295.
7. M. Wuttig and N. Yamada, *Nat. Mater.*, 2007, **6**, 824-832.
8. D. Lencer, M. Salinga and M. Wuttig, *Adv. Mater.*, 2011, **23**, 2030-2058.
9. C. E. Giusca, V. Stolojan, J. Sloan, F. Börrnert, H. Shiozawa, K. Sader, M. H. Rümmeli, B. Büchner and S. R. P. Silva, *Nano Lett.*, 2013, **13**, 4020-4027.

10. S. W. Choi, Y. Zhang and Y. Xia, *Angew. Chem. Int. Edit.*, 2010, **49**, 7904-7908.

11. G. D. Moon, S.-W. Choi, X. Cai, W. Li, E. C. Cho, U. Jeong, L. V. Wang and Y. Xia, *J. Am. Chem. Soc.*, 2011, **133**, 4762-4765.

12. D. C. Hyun, P. Lu, S. I. Choi, U. Jeong and Y. Xia, *Angew. Chem. Int. Edit.*, 2013, **52**, 10468-10471.

13. C. Wang, L. Ma, L.-M. Chen, K. X. Chai and M. Su, *Anal. Chem.*, 2010, **82**, 1838-1843.

14. C. Wang, Z. Sun, L. Ma and M. Su, *Anal. Chem.*, 2011, **83**, 2215-2219.

15. M. Su, *Nanomed.*, 2013, **8**, 253-263.

16. X. Sun, B. Yu and M. Meyyappan, *Appl. Phys. Lett.*, 2007, **90**, 183116-183116-183113.

17. Z. Ma, Y. Hong, M. Zhang and M. Su, *Appl. Phys. Lett.*, 2009, **95**, 233101.

18. B. Yoon, J. Lee, I. S. Park, S. Jeon, J. Lee and J.-M. Kim, *Journal of Materials Chemistry C*, 2013, **1**, 2388-2403.

19. B. Duong, H. Liu, L. Ma and M. Su, *Scientific reports*, 2014, **4**.

20. S.-J. Park, T. A. Taton and C. A. Mirkin, *Science*, 2002, **295**, 1503-1506.

21. J. B. Haun, T. J. Yoon, H. Lee and R. Weissleder, *Wiley Interdisciplinary Reviews: Nanomedicine and Nanobiotechnology*, 2010, **2**, 291-304.

22. D. H. Park, Y. K. Hong, E. H. Cho, M. S. Kim, D.-C. Kim, J. Bang, J. Kim and J. Joo, *ACS Nano*, 2010, **4**, 5155-5162.

23. R. L. Stoermer, J. A. Sioss and C. D. Keating, *Chem. Mater.*, 2005, **17**, 4356-4361.

24. S. R. Nicewarner-Pena, R. G. Freeman, B. D. Reiss, L. He, D. J. Peña, I. D. Walton, R. Cromer, C. D. Keating and M. J. Natan, *Science*, 2001, **294**, 137-141.

25. Z. Zhong, M. Li, D. Xiang, N. Dai, Y. Qing, D. Wang and D. Tang, *Biosens. Bioelectron.*, 2009, **24**, 2246-2249.

26. G. Bertsch, *Science*, 1997, **277**, 1619-1619.

27. A. Sharma, V. Tyagi, C. Chen and D. Buddhi, *Renew. Sust. Energ. Rev.*, 2009, **13**, 318-345.

28. L. Stappers, Y. Yuan and J. Fransaer, *J. Electrochem. Soc.*, 2005, **152**, C457-C461.

29. S. Lai, J. Guo, V. Petrova, G. Ramanath and L. Allen, *Phys. Rev. Lett.*, 1996, **77**, 99.

30. L. Liang, J. Li and Q. Jiang, *Physica B: Condensed Matter*, 2003, **334**, 49-53.

31. H. Sheng, *Philos. Mag. Lett.*, 1996, **73**, 179-186.

32. M. Zhang, M. Y. Efremov, F. Schiettekatte, E. Olson, A. Kwan, S. Lai, T. Wisleder, J. Greene and L. Allen, *Phys. Rev. B*, 2000, **62**, 10548.

33. H. Sheng, K. Lu and E. Ma, *Acta Mater.*, 1998, **46**, 5195-5205.

34. A. Lopeandia and J. Rodriguez-Viejo, *Thermochim. Acta*, 2007, **461**, 82-87.

35. M. Abtew and G. Selvaduray, *Mater. Sci. Eng. R-Rep*, 2000, **27**, 95-141.

36. H. H. Manko, *New York, NY : McGraw-Hill*, 1979, **2nd ed.**

37. Y. Peng, T. Cullis and B. Inkson, *Nano Lett.*, 2008, **9**, 91-96.

38. H. Zhang, J. Zhang, Q. Lan, H. Ma, K. Qu, B. J. Inkson, N. J. Mellors, D. Xue and Y. Peng, *Nanotechnology*, 2014, **25**, 425301.

39. J. Gibson, A. N. Goland, M. Milgram and G. Vineyard, *Phys. Rev.*, 1960, **120**, 1229.

40. M. W. Thompson, *Defects and Radiation Damage in Metals, by MW Thompson, Cambridge, UK: Cambridge University Press,* 1974, **1**.

41. T. D. de la Rubia, *Annual Review of Materials Science*, 1996, **26**, 613-649.

42. F. Banhart and P. Ajayan, *Nature*, 1996, **382**, 433-435.

43. S. Xu, M. Tian, J. Wang, J. Xu, J. M. Redwing and M. H. Chan, *Small*, 2005, **1**, 1221-1229.

44. A. Krasheninnikov and F. Banhart, *Nat. Mater.*, 2007, **6**, 723-733.

45. K. Zheng, C. Wang, Y.-Q. Cheng, Y. Yue, X. Han, Z. Zhang, Z. Shan, S. X. Mao, M. Ye and Y. Yin, *Nat. Commun.*, 2010, **1**, 24.

46. A.-A. El Mel, L. Molina-Luna, M. Buffière, P.-Y. Tessier, K. Du, C.-H. Choi, H.-J. Kleebe, S. Konstantinidis, C. Bittencourt and R. Snyders, *ACS Nano*, 2014, **8**, 1854-1861.

47. R. Egerton, P. Li and M. Malac, *Micron*, 2004, **35**, 399-409.

48. Y. Chen, R. E. Palmer and J. P. Wilcoxon, *Langmuir*, 2006, **22**, 2851-2855.

49. K.-W. Moon, W. Boettinger, U. Kattner, F. Biancaniello and C. Handwerker, *J. Electron. Mater.*, 2000, **29**, 1122-1136.

50. E. Bradley, C. A. Handwerker, J. Bath, R. D. Parker and R. W. Gedney, 2007.

Sculpting an individual nanowire with various phase status and periodicities, which may encode into a promising micro-nano identification system with the advantages of ultrahigh capacity, sustainable utilization and well stability.

39x26mm (300 x 300 DPI)